Materials Science & Engineering A 786 (2020) 139398

Contents lists available at ScienceDirect

Materials Science & Engineering A

journal homepage: http://www.elsevier.com/locate/msea

Aging- and creep-resistance of a cast hypoeutectic Al-6.9Ce-9.3Mg (wt. %) alloy

Daniel S. Ng [1], David C. Dunand [*]

Department of Materials Science and Engineering, Northwestern University, 2200 Campus Drive, Evanston, IL, 60208, USA

ARTICLE INFO

Keywords:
Al alloys
Rare earth
Precipitation hardening
Creep
Load partitioning

ABSTRACT

A ternary Al-6.9Ce-9.3Mg (wt.%) hypoeutectic alloy, consisting of equal amounts of α-Al(Mg) solid-solution regions and Al(Mg)-$Al_{11}Ce_3$ eutectic colonies, is investigated in terms of its aging and creep resistance. The eutectic regions exhibit a microhardness of 1230 MPa, which is thrice the value of Al-$Al_{11}Ce_3$ eutectic regions in a binary Al-12.5Ce (wt.%) near-eutectic alloy, demonstrating that Mg in solid-solution enhances the strengthening provided by the micron-scale highly-branched $Al_{11}Ce_3$ phase. X-ray diffraction measurements during ambient-temperature tensile testing reveal that load is being transferred from the Al(Mg) matrix to the $Al_{11}Ce_3$ phase, confirming that the fine eutectic microstructure displays composite strengthening in addition to the expected precipitation- and solid-solution strengthening. The hardness remains effectively unchanged after aging at 450 °C for up to 8 weeks, indicating excellent coarsening resistance of the $Al_{11}Ce_3$ phase. The ternary alloy exhibits creep resistance at 300 °C slightly inferior to the near-fully eutectic binary Al-12.5Ce (wt.%) alloy, consistent with the presence of large regions of fast-creeping primary Al(Mg) solid-solution matrix between the strong Al(Mg)-$Al_{11}Ce_3$ eutectic colonies in the hypoeutectic ternary alloy.

1. Introduction

Commercial precipitation-strengthened aluminum alloys are widely used in the automotive and aerospace industries for their low cost and high strength-to-weight ratio, but typically cannot be used in load-bearing applications for extended periods above ~250 °C because their nanoscale precipitates coarsen or dissolve into the aluminum matrix [1]. By contrast, the most common aluminum casting alloys, which are based on the eutectic Al-Si system [2,3], contain large Si particles that are relatively thermally stable but provide little strengthening to the surrounding fast-creeping aluminum matrix [4–7]. Recent aluminum alloy development efforts have revealed that additions of rare-earth elements (REE) improve casting behavior through increased melt fluidity, and improve mechanical properties through microstructural refinement and the formation of stable, high-melting intermetallic compounds [8,9]. A particularly inexpensive REE is cerium, which is often discarded during the refinement of more valuable REEs such as Nd and Dy, resulting in an excess Ce supply that makes it an economically feasible alloying element for aluminum, even in high-volume production [10,11].

The binary Al-Ce system has a eutectic composition at ~10 wt% (~2.1 at.%) Ce, with a fine "Chinese script" $Al_{11}Ce_3$ intermetallic phase forming upon solidification in the α-Al matrix [12]. The as-cast alloy has good mechanical properties without the need for heat treatments [13,14], and the micron-scale Al-$Al_{11}Ce_3$ microstructure is resistant to coarsening and creep deformation up to 400 °C [15]. The $Al_{11}Ce_3$ phase also exists in magnesium-aluminum-based alloys [16–18], where it similarly remains stable up to 400 °C [19]. The addition of Mg to binary Al-Ce improves casting characteristics while lowering density and providing solid-solution strengthening in the matrix [12,20]; a prior investigation into a ternary Al-8Ce-10Mg (wt.%) alloy showed significantly higher elevated-temperature strength as compared to common aluminum piston alloys [10]. The present study builds on the previous work done in evaluating the high-temperature yield and ultimate tensile strengths of the ternary Al-Ce-Mg system, which were measured at relatively high strain rates. We study here the coarsening and creep resistance (at low strain rates) of a hypoeutectic Al-6.9Ce-9.3Mg (wt.%) alloy, examine load transfer as a strengthening mechanism, and

* Corresponding author.
E-mail addresses: danielng2019@u.northwestern.edu (D.S. Ng), dunand@northwestern.edu (D.C. Dunand).
[1] Present address: Department of Materials Science and Engineering, Massachusetts Institute of Technology, 77 Massachusetts Avenue, Cambridge, MA 02139, USA.

https://doi.org/10.1016/j.msea.2020.139398
Received 9 February 2020; Received in revised form 13 April 2020; Accepted 13 April 2020
Available online 18 April 2020

compare to the behavior of the binary eutectic Al-12.5Ce (wt.%) alloy containing almost double the Ce content.

2. Experimental methods

Cast specimens with nominal composition Al-8Ce-10Mg (wt.%) were provided by Eck Industries, Inc. (Manitowoc, WI) in the homogenized state (432 °C for 6 h). The bulk composition of the alloy was measured at Genitest Inc. (Montreal, QC, Canada) to be Al-6.9Ce-9.3Mg (wt.%)—equivalent to Al-1.4Ce-10.8Mg (at.%)—using inductively-coupled plasma atomic emission spectroscopy, which also revealed expected trace amounts of Fe (0.099 wt%) and Si (0.035 wt%). An average density of 2.64 g/cm^3 was obtained via the Archimedes method, which is slightly below the alloy's theoretical density of 2.68 g/cm^3, indicating ~1.5% porosity within the specimens. The ternary alloy density is between those of eutectic Al-12.6 wt% Si (2.65 g/cm^3) [3] and pure aluminum (2.70 g/cm^3), and significantly lower than that of near-eutectic Al-12.5 wt%Ce (2.92 g/cm^3) [15].

For metallography, the as-received specimens were cut into 2 mm thick slices, mounted, and polished to a 0.3 μm surface finish. The microstructure was examined with a Hitachi SU8030 scanning electron microscope (SEM) used under an operating voltage of 25 kV and working distance of 15 mm for back-scatter imaging and energy dispersive X-ray spectroscopy (EDS). To study the microstructural stability, slices of the alloy were isothermally aged in air at 350, 400, and 450 °C for up to 8 weeks (1344 h) and terminated by water quenching. The Vickers microhardness was measured using a Duramin-5 microhardness tester, applying a 0.2 kgf load for 5 s on samples polished to a 1 μm surface finish. At least ten hardness measurements were taken and averaged for each aging time/temperature. Separate samples were used for each aging time/temperature, but all originated from the same cast specimen.

Cylindrical compressive creep samples (10 mm in diameter and 20 mm in height) were machined from the as-received specimens. Compressive creep tests were conducted in air at 300, 350 and 400 °C in a creep frame heated by a three-zone furnace. The cylindrical samples were placed between two tungsten-carbide platens inside a Ni-based superalloy compression cage lubricated with boron nitride. Each specimen was tested under a series of increasing compressive stresses, and the minimum steady-state strain rate achieved at each stress was measured using a linear variable displacement transducer (LVDT) attached to the cold end of an extensometer connected to the platens. The test for each specimen was terminated when the total accumulated strain exceeded 10%. Additionally, cylindrical dogbone tensile samples (with 5 mm gauge diameter and 32 mm gauge length) were machined from an as-received specimen. Tensile creep tests were conducted in air at 300 °C under constant stress until fracture to obtain a full strain vs. time curve as well as high-temperature tensile ductility, with strain measured using a LVDT attached to an extensometer that was clipped into grooves near the ends of the tensile specimen's gauge length.

X-ray diffraction measurements were made at Sector 1 of the Advanced Photon Source at Argonne National Laboratory (Lemont, IL). An in-situ uniaxial tensile test was performed on a small cylindrical dogbone tensile specimen (1.9 mm gauge diameter and 8.3 mm gauge length) using a screw-driven loading system with strain measured from cross-head displacement. The tensile stress on the specimen was increased in steps of 20–50 MPa and held constant while the center of the gauge length was irradiated with a monochromatic 71.7 keV (λ = 0.173 Å) beam with square cross-sectional area of 0.1 × 0.1 mm, using a sample-to-detector distance of 651 mm and a Dexela CMOS detector with 75 × 75 μm pixels. One hundred exposures, lasting 0.2 s each, were taken as the sample rotated 40° about the loading axis, and the same number were taken both 1 mm above and below the center of the gauge length for a total of 300 exposures, comprising a total diffraction volume of 0.31 mm^3. The 300 exposures for each loading condition were summed together for sufficient statistics and pseudo-Voight peak fitting was performed using the GSAS2 software package with a CeO_2 powder diffraction pattern for calibration.

3. Results and discussion

3.1. Coarsening resistance

Representative microstructures of the Al-6.9Ce-9.3Mg (wt.%) alloy in the as-received state (cast and homogenized) are shown in Fig. 1(a–c). Fig. 1(a) displays a gray α-Al(Mg) matrix containing white $Al_{11}Ce_3$ phase with an overall phase fraction of ~15%. Approximately half of the microstructure contains eutectic Al(Mg)-$Al_{11}Ce_3$ colonies, while the other half consists of precipitate-free primary α-Al(Mg) regions, which is consistent with the hypoeutectic composition of the alloy. EDS measurements revealed that the α-Al(Mg) solid-solution matrix contained 11.2 ± 0.2 wt% (12.3 ± 0.2 at.%) Mg, with the Ce content being below the EDS detection limit, consistent with the near-zero solubility of Ce in α-Al [21]. Conversely, the precipitates contained 55 ± 2 wt% (20 ± 1 at.%) Ce and no detectable Mg, with an Al:Ce atomic ratio of (80 ± 1)/(20 ± 1) = 4.0 ± 0.2 close to the stoichiometric value of 11/3 = 3.7, confirming that the phase is $Al_{11}Ce_3$ with negligible solubility of Mg.

Within the Al(Mg)-$Al_{11}Ce_3$ eutectic colonies, as illustrated in Fig. 1(b), the $Al_{11}Ce_3$ precipitates have highly-branched morphology, with branch spacings ranging from 2 to 4 μm. This is in contrast to the finer microstructure reported in the binary near-eutectic Al-12.5Ce (wt.%) alloy, which contains $Al_{11}Ce_3$ precipitates with a "Chinese script" morphology, 0.2–0.4 μm wide and several microns in length with inter-precipitate distances of ~1.5 μm [12,15]. While the $Al_{11}Ce_3$ phase is expected to provide significant ambient-temperature strengthening in eutectic regions via load transfer and precipitation strengthening [12], it may be less effective for this hypoeutectic alloy at elevated temperatures due to the large regions of fast-creeping α-Al(Mg) matrix. Casting defects, as illustrated in Fig. 1(c), with pores up to 40 μm in size comprising ~1.5% porosity in the alloy, may also adversely affect mechanical behavior, since microporosity is often responsible for crack nucleation and provides low-energy paths for crack propagation [22]. However, the casting porosity of commercial parts may be decreased through hot isostatic pressing, which has been shown to improve room-temperature mechanical properties of cast alloys with the same nominal composition, Al-8Ce-10Mg (wt.%), by increasing the yield strength from 186 to 207 MPa, the ultimate tensile strength from 228 to 262 MPa, and the elongation from 1 to 2% [10].

Coarsening resistance and retention of room-temperature mechanical properties have previously been shown in Al-Ce-Mg systems only up to 400 °C, with yield strength increasing slightly after aging for 1000 h due to homogenization of magnesium in the microstructure [10]. In this study, the alloy's microstructure after aging for 1344 h at 450 °C, as shown in Fig. 1(d), is effectively indistinguishable from the as-received specimens in Fig. 1(a–c) except for slight rounding of the $Al_{11}Ce_3$ phase, suggesting that the Al(Mg)-$Al_{11}Ce_3$ eutectic microstructure in this ternary alloy has exceptional coarsening resistance, much like in the binary Al-Ce eutectic alloy [12,15]. This is confirmed by the evolution of its Vickers microhardness during isothermal aging as shown in Fig. 2. The eutectic Al(Mg)-$Al_{11}Ce_3$ regions in the as-received Al-6.9Ce-9.3Mg alloy have a Vickers hardness of 1230 ± 70 MPa (125 ± 7 HV), with micro-indentations ~50 μm in size covering tens of $Al_{11}Ce_3$ precipitate branches. After 1344 h at 350, 400, and 450 °C, the hardness of the eutectic regions is effectively unchanged, having values of 1270 ± 70, 1270 ± 60, and 1250 ± 80 MPa, respectively, with a slight but statistically insignificant increase in hardness likely accounted for by the use of different samples for each data point.

To illustrate the exceptional thermal stability of this Al(Mg)-$Al_{11}Ce_3$ microstructure, the evolution of Vickers microhardness for several other aluminum alloys is also shown for comparison in Fig. 2. As expected, the hardness of the binary near-eutectic Al-12.5Ce alloy is also unaffected by aging at 400 °C for up to 12 weeks, although its hardness is significantly

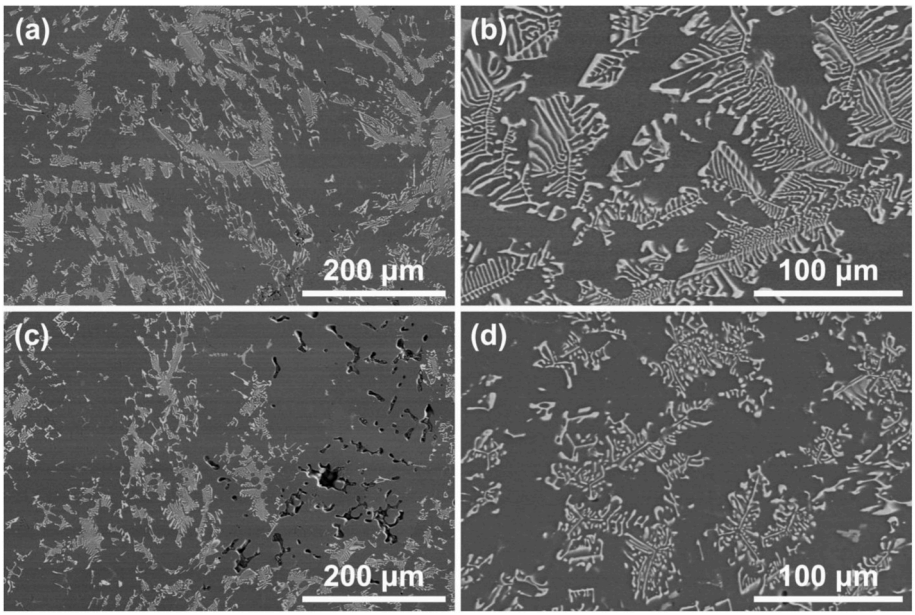

Fig. 1. Scanning electron micrographs of Al-6.9Ce-9.3Mg (wt.%) cross-sections, showing (a) representative microstructure of as-received alloy with α-Al(Mg) matrix and eutectic Al(Mg)-$Al_{11}Ce_3$ regions, (b) detail of fine eutectic Al(Mg)-$Al_{11}Ce_3$ with micron-scale eutectic structure, (c) casting porosity, and (d) after aging for 8 weeks at 450 °C.

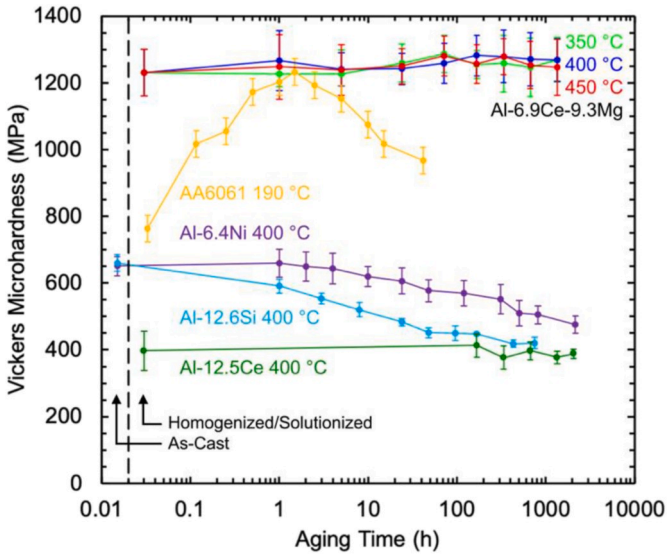

Fig. 2. Vickers microhardness of eutectic Al(Mg)-$Al_{11}Ce_3$ regions in the Al-6.9Ce-9.3Mg (wt.%) alloy as a function of isothermal aging time at 350, 400, and 450 °C for up to 8 weeks (1344 h). For comparison, the evolution of microhardness is shown for the commercial precipitation-strengthened aluminum alloy 6061 at 190 °C [23], and the binary eutectic aluminum alloys Al-Ni [24], Al-Si [15], and Al-Ce [15] at 400 °C. Before aging, the Ce-containing alloys were homogenized for 6 h at 432 °C, and the 6061 alloy was solutionized for 20 min at 560 °C.

lower than that of the eutectic regions in the ternary alloy studied here. The commercial precipitation-strengthened aluminum alloy 6061 exhibits a strong age-hardening effect [23], with a solutionized hardness increasing by over 400 MPa to reach peak hardness in just 1 h at 190 °C, after which it becomes overaged. Data for the binary eutectic alloys Al-6.4Ni [24] and Al-12.6Si [15] (wt.%) show that although they are not age-hardenable, their eutectic microstructures are not as coarsening-resistant at 400 °C compared to the $Al_{11}Ce_3$-containing alloys, with a 150 MPa drop in hardness after 816 h (5 weeks) for Al-6.4Ni and a 240 MPa drop after 751 h (4.5 weeks) for Al-12.6Si.

The high hardness (1230 ± 70 MPa) of the eutectic regions of the Al-6.9Ce-9.3Mg alloy, especially as compared to the binary Al-Ce eutectic with a hardness lower by a factor of three, is largely attributable to solid-solution strengthening from Mg additions. Even hardness measurements taken in primary α-Al(Mg) matrix regions without any visible $Al_{11}Ce_3$ phase resulted in high values of 1000 ± 60 MPa, which also remained unchanged after 8 weeks at 450 °C. However, this value may be artificially increased due to eutectic colonies beneath or around the micro-indentation affecting the local strain field. Indeed, a binary Al-11.2 Mg wt.% solid-solution strengthened alloy is expected to have a Vickers microhardness of ~690 MPa [20], well below this study's measured value of 1000 ± 60 MPa.

The strength increment provided by the $Al_{11}Ce_3$ phase can be approximated as ΔHV/3 [25], where ΔHV is the difference between the microhardness of the eutectic regions (1230 ± 70 MPa) and that of the α-Al(Mg) matrix (690 MPa). The resulting value, 180 ± 30 MPa, is significantly larger than the strength increment provided by the $Al_{11}Ce_3$ in the binary Al-12.5Ce alloy, 67 ± 20 MPa, likely due to differences in the eutectic microstructure. While binary Al-12.5Ce has a higher overall phase fraction of $Al_{11}Ce_3$ in the alloy, the phase fraction of $Al_{11}Ce_3$ within the eutectic colonies, where microhardness measurements were taken, is significantly lower (~20% for Al-12.5Ce vs. ~30% for Al-6.9Ce-9.3Mg, as measured from metallographic cross-sections). Furthermore, the highly branched architecture of the $Al_{11}Ce_3$ phase in the ternary alloy may provide more effective matrix strengthening than the Chinese-script structure of the $Al_{11}Ce_3$ precipitates in the binary alloy. The ternary Al-6.9Ce-9.3Mg alloy's coarser eutectic microstructure compared to the binary Al-12.5Ce alloy suggests a smaller strengthening contribution provided by the Orowan strengthening mechanism in the ternary alloy [26]. However, previous work on the binary Al-12.5Ce alloy concluded that the Orowan mechanism only accounts for a small portion of the strength increment between the Al-$Al_{11}Ce_3$ eutectic microstructure and a pure Al matrix [15], suggesting that other strengthening effects such as load transfer play a significant role [12].

3.2. Creep properties

A double-logarithmic plot of steady-state creep strain rate vs. applied stress is shown in Fig. 3(a) for Al-6.9Ce-9.3Mg tested at 300, 350, and 400 °C. Filled-in circular and triangular data points represent tests on two separate samples at each temperature, with slight differences between repeat experiments most likely explained by differences in microstructure due to variations in cooling rates in the as-cast specimens from which the creep samples were machined. The two hollow green data points plotted in Fig. 3(a) represent tensile creep results at 300 °C.

In Fig. 3(b), the creep response for Al-6.9Ce-9.3Mg at 350 °C is compared to those of two binary alloys at the same temperature: solid-solution strengthened Al-5.0Mg at low (<10 MPa) and intermediate (20–70 MPa) stresses [27], and near-eutectic Al-12.5Ce [15]. All of the creep curves in Fig. 3 are fitted to the power-law equation:

$$\dot{\varepsilon} = A\sigma^n \exp\left(\frac{-Q}{RT}\right) \quad (1)$$

where $\dot{\varepsilon}$ is the steady-state strain rate, A is a dimensionless constant, σ is the stress, n is the stress exponent, Q is the activation energy, R is the gas constant, and T is the absolute temperature. The stress exponents for Al-6.9Ce-9.3Mg are all similar, ranging from $n = 4.6 \pm 0.3$ to $n = 5.2 \pm 0.5$, suggesting similar deformation mechanisms at the three different temperatures. As seen in Fig. 3(b), the ternary Al-6.9Ce-9.3Mg alloy exhibits creep resistance at 350 °C that is superior to the binary Al-5.0Mg solid-solution strengthened alloy, but inferior to the binary Al-12.5Ce near-eutectic alloy. The improvement over Al-5.0Mg is likely due to a combination of increased solid-solution strengthening from a higher Mg content and the fine $Al_{11}Ce_3$ phase providing load-transfer reinforcement in the eutectic colonies. However, the limited fraction of these eutectic colonies (~50 vol%) in the ternary alloy likely limits the effectiveness of the $Al_{11}Ce_3$ phase, as the fast-creeping α-Al(Mg) primary regions deform around eutectic Al(Mg)-$Al_{11}Ce_3$ colonies, which explains the superiority of the near-eutectic Al-12.5Ce alloy without primary Al regions, despite its lack of solid-solution strengthening.

Binary solid-solution strengthened alloys such as Al-Mg are expected to have stress exponents in the range 4–5 at low stresses (as observed in Fig. 3(b)), behaving similarly to pure Al, which has $n = 4.4$ with dislocation climb as the rate-controlling mechanism [28,29]. While the stress exponents of n ~5 for the ternary Al-6.9Ce-9.3Mg alloy appear to fall into this range, the ternary alloy maintains its stress exponent well above 10 MPa. This is in contrast to the behavior of the binary solid-solution strengthened alloy at intermediate stresses, where the stress exponent drops to $n = 3.1 \pm 0.2$ as dislocation glide is slowed down by the formation of clouds of solute atoms around dislocations, causing glide ($n = 3$) to become the rate-controlling factor [28]. On the other hand, while the binary near-eutectic Al-Ce alloy also exhibits a stress exponent close to that of pure Al with $n = 4.7 \pm 0.7$ for low stresses, it displays a much higher stress exponent of $n = 9.0 \pm 0.2$ above a threshold stress of ~14 MPa at 350 °C, when dislocation creep begins to be inhibited by the $Al_{11}Ce_3$ precipitates [15].

In contrast, the ternary Al-6.9Ce-9.3Mg alloy does not exhibit any change in stress exponent over the full range (five orders of magnitude) of strain rates. The fact that both its steady-state strain rate and its stress exponent lie between the corresponding values for the binary Al-5.0Mg and Al-12.5Ce alloys suggests that the deformation mechanism involves a combination of contributions from Mg solid-solution strengthening and $Al_{11}Ce_3$ precipitate strengthening. Although the stress exponents of n ~5 could indicate that dislocation climb is the primary deformation mechanism in the ternary alloy even at intermediate stresses, this is unlikely given the high activation energy, which is calculated by rearranging Eq. (1) into

$$Q = -R\frac{d\ln\dot{\varepsilon}}{d(1/T)} \quad (2)$$

Using strain rates calculated from the best fit-lines in Fig. 3(a) at 15 MPa, an activation energy of $Q = 246 \pm 23$ kJ/mol is determined from the slope in Fig. 4(a). This is significantly higher than both the value of 142 kJ/mol for pure Al creep [30] and 130 kJ/mol for diffusion of Mg in Al [4], and is in fact much closer to the activation energy 215 ± 18 kJ/mol determined for the Al-12.5Ce alloy at 35 MPa [15]. We can therefore conclude that the eutectic Al(Mg)-$Al_{11}Ce_3$ microstructure is likely playing a significant, if not primary, role in the ternary Al-6.9Ce-9.3Mg alloy's creep behavior by inhibiting dislocation motion.

Fig. 4(b) shows the evolution of strain as a function of time for an Al-6.9Ce-9.3Mg specimen crept in tension until failure at 300 °C under a constant stress of 13 MPa. The alloy exhibits primary, secondary, and tertiary creep, a steady-state strain rate of 2.5×10^{-8} s^{-1}, and

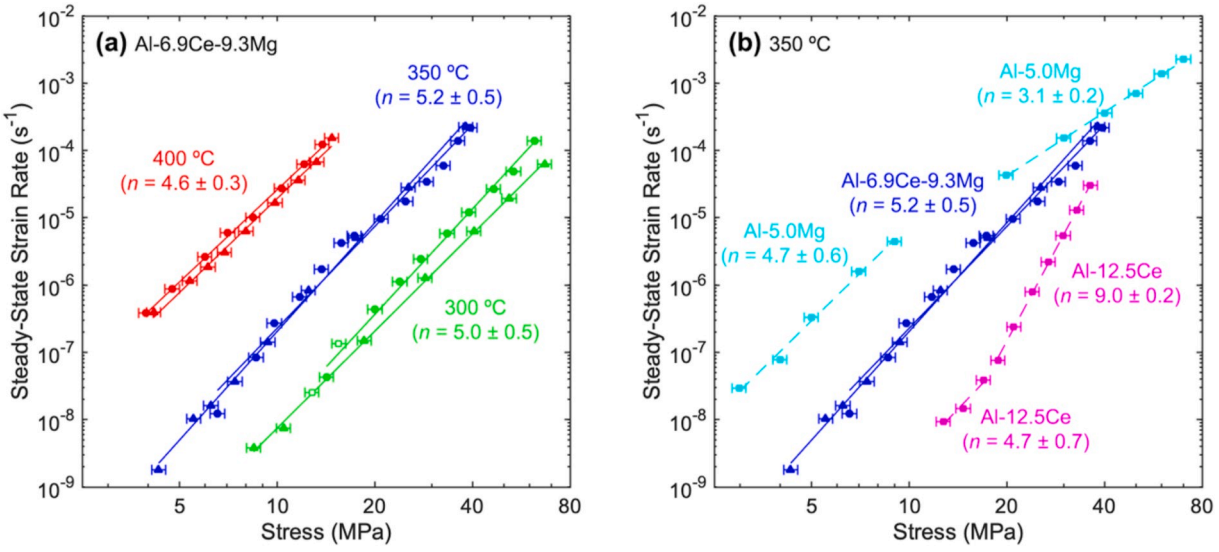

Fig. 3. Double-logarithmic plots of minimum steady-state strain rate vs. stress for (a) Al-6.9Ce-9.3Mg specimens crept at 300, 350 and 400 °C labelled with stress exponents n in parentheses. Filled in circles and triangles represent data from two different compressive samples at each temperature, and two hollow data points are shown for tensile creep at 300 °C. For comparison, literature data for creep at 350 °C are shown in (b) with dotted lines for solid-solution strengthened Al-5.0Mg (in tension, from Ref. [27]) and eutectic Al–12.5Ce (in compression, from Ref. [15]), with two stress exponents given for each alloy, representing distinct deformation mechanisms at low and intermediate stresses. Compressive creep data for Al-6.9Ce-9.3Mg are between those of the two binary alloys.

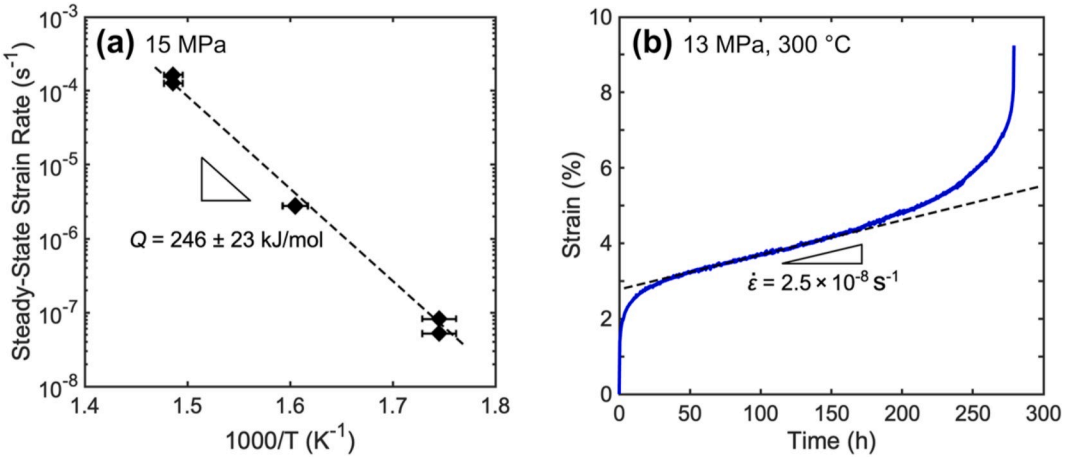

Fig. 4. (a) Arrhenius plot of compressive creep steady-strain rate vs. reciprocal temperature at 15 MPa for Al-6.9Ce-9.3Mg, showing best-fit line for creep activation energy Q, and (b) plot of tensile creep strain vs. time at 300 °C under a constant stress of 13 MPa, showing minimum steady-state strain rate.

reasonable creep ductility, achieving just over 9% elongation before fracture. The strain rate for this tensile creep test is also plotted as one of the hollow data points in Fig. 3(a), from which it is apparent that the tensile creep performance of this alloy is not significantly different from its compressive creep performance despite some porosity in the cast samples.

Fig. 5 shows the cross-sectional microstructure of the Al-6.9Ce-9.3Mg alloy after creep tests at 300 °C, with Fig. 5(a) being representative of the alloy with 8% accumulated compressive strain, and Fig. 5 (b) with 9% accumulated tensile strain within the gauge length, but imaged away from the fracture surface. In both micrographs, it appears that the $Al_{11}Ce_3$ microstructure is effectively identical to the as-received state in Fig. 1(a), confirming the high thermal stability of the microstructure even under applied external stresses. However, the microstructure near the tensile fracture surface, illustrated in Fig. 5(c), shows that the $Al_{11}Ce_3$ phase is aligned along the tensile axis, likely due to high local plastic strain in the necking region. Furthermore, there is cavitation in the matrix near the fracture surface shown in Fig. 5(d), and small pores at the Al(Mg)-$Al_{11}Ce_3$ interfaces suggest that there are differences in the deformation behavior of the two phases, which ultimately leads to macroscopic failure as the cavities act as stress concentrators for crack initiation and propagation.

3.3. X-ray diffraction under load

Fig. 6(a) displays the diffraction pattern from the summation of exposures for Al-6.9Ce-9.3Mg under zero load at room temperature, with distinct diffraction rings for both the α-Al(Mg) matrix (FCC, $a = 4.1$ Å [31]) and $Al_{11}Ce_3$ phase (orthorhombic *Immm*, $a = 4.4$ Å, $b = 13.0$ Å, $c = 10.1$ Å [32]). The speckled nature of the diffraction rings indicates that the number of grains within the diffracted volume of 0.31 mm^3 is not very large. Based on the size of the primary α-Al(Mg) and eutectic regions in Fig. 1(a,b), a lower-bound estimate for the grain size is ~0.2 mm, corresponding to an upper bound of ~40 grains in the diffracted volume, which is consistent with the ring's speckled appearance.

The application of uniaxial tensile stress increases the lattice spacing parallel to the loading axis and, by the Poisson effect, decreases the lattice spacing perpendicular to the loading axis, thereby distorting the

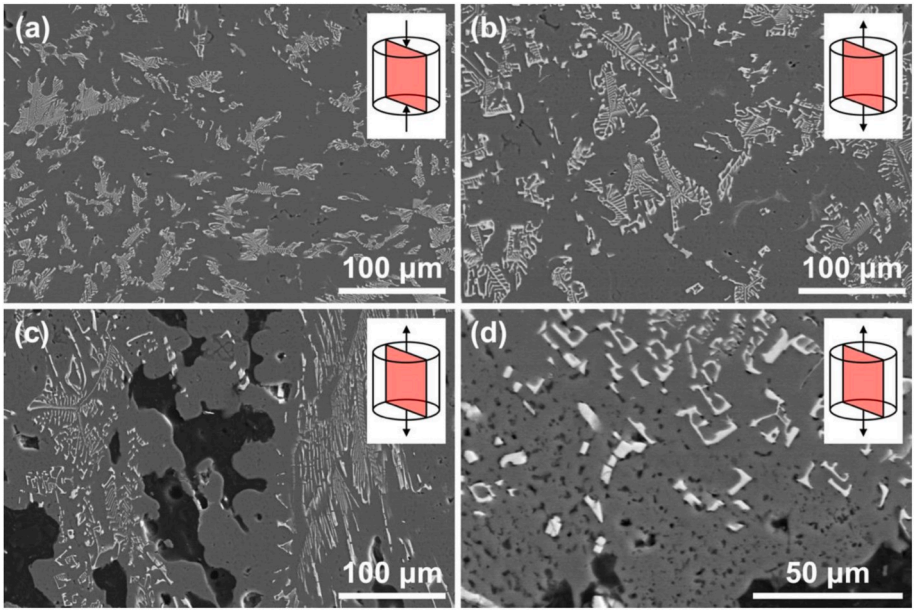

Fig. 5. Scanning electron micrographs of Al-6.9Ce-9.3Mg cross-sections (a) after compressive creep at 300 °C, with 8% accumulated strain and (b) after tensile creep until failure at 300 °C, with 9% accumulated strain, ~2 mm away from the fracture surface, (c) next to the tensile fracture surface, where black mounting material has filled in the rough areas of the fracture surface, and (d) cavitation near the tensile fracture surface (at higher magnification).

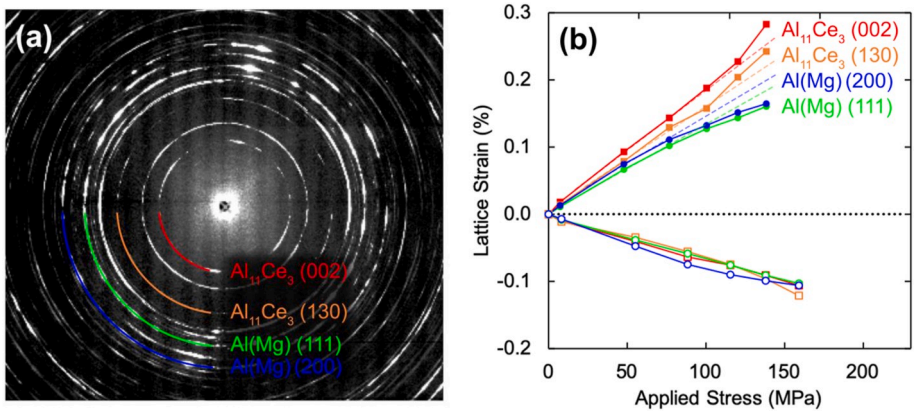

Fig. 6. (a) Summed diffraction pattern of Al-6.9Ce-9.3Mg under zero stress at ambient temperature, with studied lattice reflections labelled and (b) plot of lattice strain vs. applied tensile stress for Al(Mg) and $Al_{11}Ce_3$ phases at ambient temperature, with filled data points indicating positive axial strains and hollow data points indicating negative transverse strains. Dotted lines are added to show deviations from initial linear elastic behavior.

circular diffraction rings into ellipses [33]. The diffraction pattern in Fig. 6(a) is oriented such that the minor diameter of the slightly elliptical rings in the vertical direction corresponds to the lattice spacing parallel to the tensile loading axis, while the major diameter in the horizontal direction corresponds to the lattice spacing along the transverse axis.

The $Al_{11}Ce_3$ (002) and (130) and the Al(Mg) (111) and (200) lattice reflections were selected for ellipse fitting, as they exhibited the highest intensities among the reflections with non-overlapping peaks. Their corresponding lattice spacings d along the axial and transverse loading directions were determined for the summed diffraction patterns at each applied tensile stress. By comparing with the unstressed lattice spacing d_0, the axial and transverse lattice strains $\varepsilon = (d - d_0)/d_0$ were determined as a function of the tensile stress applied to the specimen, as shown in Fig. 6(b).

The Al(Mg) matrix has similar lattice strains for both the (111) and (200) lattice plane spacings, which is expected from aluminum's nearly isotropic cubic crystal structure [34]. However, the $Al_{11}Ce_3$ phase exhibits somewhat greater axial lattice strain for the (002) spacing than for the (130) spacing, which is consistent with its orthorhombic crystal structure being anisotropic, as determined from first-principles calculations [35]. Furthermore, the $Al_{11}Ce_3$ phase has a greater axial lattice strain for both reflections as compared to the Al(Mg) matrix, indicating non-isostrain behavior caused by unequal load partitioning between the two phases. The average microstress in each phase (as opposed to the macroscopic applied stress) can be calculated as the product of the lattice strain ε and the elastic diffraction constant E. Assuming that the elastic diffraction constant of each phase can be approximated by their respective Young's modulus, the solid-solution-strengthened Al(Mg) matrix has a value of $E = 71$ GPa [36], while the $Al_{11}Ce_3$ phase is 65% stiffer with $E = 117$ GPa, from first-principles calculations [35]. Then for a given macroscopic loading condition, $Al_{11}Ce_3$ has both a greater lattice strain and a higher elastic diffraction constant than Al(Mg) does, and therefore the microstress in the $Al_{11}Ce_3$ phase is considerably greater than in the Al(Mg) matrix. For the highest applied stress of 138 MPa in Fig. 6(b), the average axial stress on the two phases are 115 MPa for Al (Mg) and 307 MPa for $Al_{11}Ce_3$. As compared to the applied stress, the matrix is under-loaded while the $Al_{11}Ce_3$ phase is overloaded, as expected if load transfer is operating between the two phases.

In contrast to the axial lattice strains, the transverse strains shown in Fig. 6(b) are similar for both the Al(Mg) matrix and $Al_{11}Ce_3$ phases, suggesting a smaller degree of load-sharing. Nevertheless, due to the greater stiffness of the $Al_{11}Ce_3$ phase, the equi-strain behavior still indicates that $Al_{11}Ce_3$ carries a greater microstress than the matrix. The $Al_{11}Ce_3$ phase's larger axial strain but equal transverse strain relative to the matrix is consistent with $Al_{11}Ce_3$ having a smaller Poisson's ratio of 0.24 (based on first-principles calculations) [35] as compared to 0.34 for Al [37]. However, finite-element modeling calculations will be required to fully understand the stress tensor of the alloy's complex microstructure.

Given the yield stress of 186 MPa for as-cast Al-8Ce-10Mg [10], the data in Fig. 6(b) are expected to belong to the macroscopically linear-elastic region. However, there is a downward deviation from the linear lattice strain (and therefore microstress) vs. applied stress response for the Al(Mg) matrix under applied stresses exceeding ~100 MPa. This suggests that the matrix phase is yielding and shedding stress to the stronger, elastic $Al_{11}Ce_3$ phase, as reported in metal matrix composites where the matrix achieves plasticity before the reinforcement [38–41]. The expected concomitant upward deviation from the linear strain-stress curve for the $Al_{11}Ce_3$ phase is indeed visible in Fig. 6 (b). This behavior is consistent with a previous neutron diffraction study suggesting that there is significant load partitioning to the $Al_{11}Ce_3$ phase in near-eutectic Al-12Ce and Al-12Ce-0.4Mg alloys during uniaxial compression [12]. These authors mostly investigated the plastic region of the Al-12Ce-0.4Mg alloy at much higher macroscopic strains, showing two data points on loading in the elastic range of the alloy for compressive stresses of 0 and 20 MPa, and multiple data points upon elastic unloading (from 131 to 0 MPa) following deformation in the plastic range of the alloy. They find an apparent Young's modulus of 78 GPa for the Al(Mg) matrix (no data are reported for $Al_{11}Ce_3$), which is comparable to our value of 73 GPa determined from the first four data points for the Al(Mg) (200) lattice strain upon tensile loading, as shown by the blue dotted line in Fig. 6(b). The slight discrepancy can be assigned to differences in Mg content and $Al_{11}Ce_3$ volume fraction between the two alloys.

This evidence for load transfer is also consistent with the large ambient-temperature strength increment provided by the $Al_{11}Ce_3$ phase to the matrix. Furthermore, as the thermally-activated plastic deformation of the matrix phase is strongly accelerated at elevated temperatures, the high-melting (and thus slow-creeping) $Al_{11}Ce_3$ is especially important as a reinforcing phase to take on a greater proportion of the load shed by the rapidly-creeping matrix, consistent with our prior discussion of load transfer during creep deformation.

4. Conclusions

The present research investigates the coarsening resistance and mechanical properties of a cast Al-6.9Ce-9.3Mg (wt.%) hypoeutectic alloy consisting of an α-Al matrix with Mg in solid solution, and embedded eutectic colonies containing a fine distribution of highly-branched $Al_{11}Ce_3$ phase, with a volume fraction of ~15% (when averaged over the whole sample).

- The Al(Mg)-$Al_{11}Ce_3$ eutectic microstructure in the ternary alloy has a high Vickers microhardness of 1230 ± 70 MPa, likely due to a combination of (i) solid-solution strengthening from a high (11.2 wt %) Mg content in the matrix, (ii) precipitation strengthening from the $Al_{11}Ce_3$ phase, and (iii) load-transfer strengthening from the $Al_{11}Ce_3$ phase. The ternary eutectic hardness is much higher than that of the binary near-eutectic Al-12.5Ce alloy (400 ± 60 MPa).
- Microhardness and morphology of the Al(Mg)-$Al_{11}Ce_3$ eutectic regions remain effectively unchanged after 8 weeks (1344 h) at temperatures up to 450 °C, demonstrating excellent coarsening resistance.
- Creep resistance of the ternary Al-6.9Ce-9.3Mg alloy is superior to that of an Al-5.0Mg solid-solution strengthened alloy but inferior to an Al-12.5Ce near-eutectic alloy. A creep activation energy of 246 ± 23 kJ/mol—much higher than the value for dislocation creep but similar to that of the Al-12.5Ce near-eutectic alloy—suggests that the eutectic microstructure plays a significant role in creep behavior, via both precipitate- and composite strengthening, consistent with the hypoeutectic ternary alloy's intermediate creep performance.
- The ternary alloy remains microstructurally stable after accumulating up to 9% creep strain at 300 °C, with similar steady-state creep strain rates in both compression and tension.
- Ambient-temperature synchrotron x-ray diffraction experiments in the elastic range of tensile loading suggest that the Al(Mg) matrix yields before the $Al_{11}Ce_3$ second phase and that the applied stress partitions between matrix and intermetallic phase, revealing the importance of the eutectic microstructure to exploit load transfer as an effective strengthening mechanism. Increasing the Ce content in the ternary alloy towards the Al(Mg)-$Al_{11}Ce_3$ eutectic composition is expected to further improve both ambient- and elevated-temperature mechanical performance.

Data availability

The raw/processed data required to reproduce these findings cannot be shared online at this time due to technical or time limitations.

Declaration of competing interest

The authors declare the following financial interests/personal relationships which may be considered as potential competing interests: DCD discloses that they have a financial interest in Braidy Industries, which commercializes various aluminum alloys.

CRediT authorship contribution statement

Daniel S. Ng: Investigation, Writing - original draft, Visualization. **David C. Dunand:** Conceptualization, Writing - review & editing, Supervision.

Acknowledgements

DSN received support from the Combat Capabilities Development Command - Army Research Laboratory via the Army Educational Outreach Program. The authors thank Dr. David Weiss from Eck Industries, Inc. for providing the cast Al-Ce-Mg alloys, Dr. Jun-Sang Park for support during measurements at the 1-ID-C beamline of the Advanced Photon Source (APS) and Dr. Jon Erik Mogonye (ARL) for numerous useful discussions. The use of APS, an Office of Science User Facility operated by Argonne National Laboratory, was supported by the U.S. DOE under contract DE-AC02-06CH11357. This work made use of the Materials Characterization and Imaging Facility at Northwestern University, which receives support from the MRSEC Program (NSF DMR-1720139) of the Materials Research Center at Northwestern University. This work made also use of the EPIC facility of Northwestern University's NUANCE Center, which has received support from the Soft and Hybrid Nanotechnology Experimental (SHyNE) Resource (NSF ECCS-1542205); the MRSEC Program; the International Institute for Nanotechnology (IIN); the Keck Foundation; and the State of Illinois, through the IIN.

Appendix A. Supplementary data

Supplementary data related to this article can be found at https://doi.org/10.1016/j.msea.2020.139398.

References

[1] J.G. Kaufman, E.L. Rooy, Aluminum Alloy Castings: Properties, Processes, and Applications, ASM International, Materials Park, OH, 2004.
[2] S. Otarawanna, A.K. Dahle, Casting of aluminium alloys, in: Fundam. Alum. Metall., Elsevier, 2011, pp. 141–154, https://doi.org/10.1533/9780857090256.1.141.
[3] S.P. Nikanorov, M.P. Volkov, V.N. Gurin, YuA. Burenkov, L.I. Derkachenko, B. K. Kardashev, L.L. Regel, W.R. Wilcox, Structural and mechanical properties of Al–Si alloys obtained by fast cooling of a levitated melt, Mater. Sci. Eng. 390 (2005) 63–69, https://doi.org/10.1016/j.msea.2004.07.037.
[4] S. Spigarelli, M. Cabibbo, E. Evangelista, S. Cucchieri, Evaluation of the creep properties of an Al–17Si–1Mg–0.7Cu alloy, Mater. Lett. 56 (2002) 1059–1063, https://doi.org/10.1016/S0167-577X(02)00677-8.
[5] G. Requena, H.P. Degischer, Creep behaviour of unreinforced and short fibre reinforced AlSi12CuMgNi piston alloy, Mater. Sci. Eng. 420 (2006) 265–275, https://doi.org/10.1016/j.msea.2006.01.024.
[6] T. Jaglinski, R. Lakes, Creep behavior of Al-Si die-cast alloys, J. Eng. Mater. Technol. 126 (2004) 378–383, https://doi.org/10.1115/1.1789953.
[7] L. Zuo, B. Ye, J. Feng, X. Kong, H. Jiang, W. Ding, Microstructure, tensile properties and creep behavior of Al-12Si-3.5Cu-2Ni-0.8Mg alloy produced by different casting technologies, J. Mater. Sci. Technol. 34 (2018) 1222–1228, https://doi.org/10.1016/j.jmst.2017.06.011.
[8] S. Alkahtani, E. Elgallad, M. Tash, A. Samuel, F. Samuel, Effect of rare earth metals on the microstructure of Al-Si based alloys, Materials 9 (2016) 45, https://doi.org/10.3390/ma9010045.
[9] F. Czerwinski, Cerium in aluminum alloys, J. Mater. Sci. (2019), https://doi.org/10.1007/s10853-019-03892-z.
[10] D. Weiss, Improved high-temperature aluminum alloys containing cerium, J. Mater. Eng. Perform. 28 (2019) 1903–1908, https://doi.org/10.1007/s11665-019-3884-2.
[11] R.T. Nguyen, D.D. Imholte, O.R. Rios, D. Weiss, Z. Sims, E. Stromme, S.K. McCall, Anticipating impacts of introducing aluminum-cerium alloys into the United States automotive market, Resour. Conserv. Recycl. 144 (2019) 340–349, https://doi.org/10.1016/j.resconrec.2019.02.009.
[12] Z.C. Sims, O.R. Rios, D. Weiss, P.E.A. Turchi, A. Perron, J.R.I. Lee, T.T. Li, J. A. Hammons, M. Bagge-Hansen, T.M. Willey, K. An, Y. Chen, A.H. King, S. K. McCall, High performance aluminum–cerium alloys for high-temperature applications, Mater. Horiz. 4 (2017) 1070–1078, https://doi.org/10.1039/C7MH00391A.
[13] E.T. Stromme, H.B. Henderson, Z.C. Sims, M.S. Kesler, D. Weiss, R.T. Ott, F. Meng, S. Kassoumeh, J. Evangelista, G. Begley, O. Rios, Ageless aluminum-cerium-based alloys in high-volume die casting for improved energy efficiency, JOM 70 (2018) 866–871, https://doi.org/10.1007/s11837-018-2861-9.
[14] D. Weiss, Castability and characteristics of high cerium aluminum alloys, in: T. R. Vijayaram (Ed.), Adv. Cast. Technol., InTech, 2018, https://doi.org/10.5772/intechopen.72830.
[15] Y. Liu, R.A. Michi, D.C. Dunand, Cast near-eutectic Al-12.5 wt.% Ce alloy with high coarsening and creep resistance, Mater. Sci. Eng. 767 (2019) 138440, https://doi.org/10.1016/j.msea.2019.138440.
[16] Y.L. Song, Y.H. Liu, S.H. Wang, S.R. Yu, X.Y. Zhu, Effect of cerium addition on microstructure and corrosion resistance of die cast AZ91 magnesium alloy, Mater. Corros. 58 (2007) 189–192, https://doi.org/10.1002/maco.200603988.
[17] K.N. Braszczyńska-Malik, E. Przełożyńska, Microstructure of Mg–Al–RE-type experimental magnesium alloy gravity cast into sand mould, Arch. Foundry Eng. 16 (2016) 115–118, https://doi.org/10.1515/afe-2016-0037.
[18] A. Wu, C. Xia, S. Wang, Effects of cerium on the microstructure and mechanical properties of AZ31 alloy, Rare Met. 25 (2006) 371–376, https://doi.org/10.1016/S1001-0521(06)60070-3.
[19] W. Wang, J. Zhang, G. Li, Y. Feng, M. Su, Y. Jiao, R. Wu, Z. Zhang, Microstructural stability of heat-resistant high-pressure die-cast Mg-4Al-4Ce alloy, Int. J. Mater. Res. 108 (2017) 427–430, https://doi.org/10.3139/146.111486.
[20] Y. Souilah, A. Boutouta, S. Boulkhessaim, H. Bedboudi, A. Bourbia, M. Draissia, Correlation of hardness and corrosion characteristics with crystalline structures of Al–Mg alloys, Phys. Scripta 88 (2013), 065601, https://doi.org/10.1088/0031-8949/88/06/065601.
[21] C. Weiping, Diffusion of cerium in the aluminium lattice, J. Mater. Sci. Lett. 16 (1997) 1824–1826, https://doi.org/10.1023/A:1018572803223.
[22] J.M. Boileau, J.E. Allison, The effect of solidification time and heat treatment on the fatigue properties of a cast 319 aluminum alloy, Metall. Mater. Trans. 34 (2003) 1807–1820, https://doi.org/10.1007/s11661-003-0147-4.

[23] A. Bahrami, M. Yazdan Mehr, Modeling electrical resistivity of naturally aged Al–Mg–Si alloys, Metals 9 (2019) 310, https://doi.org/10.3390/met9030310.
[24] R.A. Michi, J.P. Toinin, D.N. Seidman, D.C. Dunand, Ambient- and elevated-temperature strengthening by Al3Zr-Nanoprecipitates and Al3Ni-Microfibers in a cast Al-2.9Ni-0.11Zr-0.02Si-0.005Er (at.%) alloy, Mater. Sci. Eng. 759 (2019) 78–89, https://doi.org/10.1016/j.msea.2019.05.018.
[25] P. Zhang, S.X. Li, Z.F. Zhang, General relationship between strength and hardness, Mater. Sci. Eng. 529 (2011) 62–73, https://doi.org/10.1016/j.msea.2011.08.061.
[26] Z. Zhang, D. Chen, Consideration of Orowan strengthening effect in particulate-reinforced metal matrix nanocomposites: a model for predicting their yield strength, Scripta Mater. 54 (2006) 1321–1326, https://doi.org/10.1016/j.scriptamat.2005.12.017.
[27] M. Pahutová, J. Čadek, On two types of creep behaviour of F.C.C. solid solution alloys, Phys. Status Solidi 56 (1979) 305–313, https://doi.org/10.1002/pssa.2210560133.
[28] S. Spigarelli, C. Paoletti, A unified physical model for creep and hot working of Al-Mg solid solution alloys, Metals 8 (2017) 9, https://doi.org/10.3390/met8010009.
[29] F.A. Mohamed, Creep behavior of solid solution alloys, Mater. Sci. Eng. 38 (1979) 73–80, https://doi.org/10.1016/0025-5416(79)90034-X.
[30] T.S. Lundy, J.F. Murdock, Diffusion of Al ^{26} and Mn ^{54} in aluminum, J. Appl. Phys. 33 (1962) 1671–1673, https://doi.org/10.1063/1.1728808.
[31] D.H. Jang, Y.B. Park, W.J. Kim, Significant strengthening in superlight Al-Mg alloy with an exceptionally large amount of Mg (13 wt%) after cold rolling, Mater. Sci. Eng. 744 (2019) 36–44, https://doi.org/10.1016/j.msea.2018.11.132.
[32] J.X. Boucherle, F. Givord, G. Lapertot, A. Muñoz, J. Schweizer, The magnetic structures of Ce3Al11: a single crystal study, J. Magn. Magn Mater. 148 (1995) 397–408, https://doi.org/10.1016/0304-8853(95)00051-8.
[33] D.K. Balch, E. Üstündag, D.C. Dunand, Elasto-plastic load transfer in bulk metallic glass composites containing ductile particles, Metall. Mater. Trans. 34 (2003) 1787–1797, https://doi.org/10.1007/s11661-003-0145-6.
[34] T.H. Courtney, Mechanical Behavior of Materials, second ed., McGraw Hill, Boston, 2000.
[35] W.-J. Ding, J.-X. Yi, P. Chen, D.-L. Li, L.-M. Peng, B.-Y. Tang, Elastic properties and electronic structures of typical Al–Ce structures from first-principles calculations, Solid State Sci. 14 (2012) 555–561, https://doi.org/10.1016/j.solidstatesciences.2012.02.006.
[36] K. Abe, Y. Tanji, H. Yoshinaga, S. Morozumi, Young's modulus of an Al-Mg alloy at elevated temperatures, J. Jpn. Inst. Light Metals 27 (1977) 279–281, https://doi.org/10.2464/jilm.27.279.
[37] C. Comte, J. von Stebut, Microprobe-type measurement of Young's modulus and Poisson coefficient by means of depth sensing indentation and acoustic microscopy, Surf. Coating. Technol. 154 (2002) 42–48, https://doi.org/10.1016/S0257-8972(01)01706-6.
[38] M.L. Young, J.D. Almer, M.R. Daymond, D.R. Haeffner, D.C. Dunand, Load partitioning between ferrite and cementite during elasto-plastic deformation of an ultrahigh-carbon steel, Acta Mater. 55 (2007) 1999, https://doi.org/10.1016/j.actamat.2006.11.004. –2011.
[39] E. Maire, A. Owen, J.-Y. Buffiere, P.J. Withers, A synchrotron X-ray study of a Ti/SiCf composite during in situ straining, Acta Mater. 49 (2001) 153–163, https://doi.org/10.1016/S1359-6454(00)00218-4.
[40] J.C. Hanan, E. Üstündag, I.J. Beyerlein, G.A. Swift, J.D. Almer, U. Lienert, D. R. Haeffner, Microscale damage evolution and stress redistribution in Ti–SiC fiber composites, Acta Mater. 51 (2003) 4239–4250, https://doi.org/10.1016/S1359-6454(03)00240-4.
[41] A. Wanner, D.C. Dunand, Synchrotron X-ray study of bulk lattice strains in externally loaded Cu-Mo composites, Metall. Mater. Trans. 31 (2000) 2949–2962, https://doi.org/10.1007/BF02830344.